Radiation stability of nanocrystalline single phase multicomponent alloys

E. Levo*[1], F. Granberg†[1], D. Utt[2], K. Albe[2], K. Nordlund[1], and F. Djurabekova[3,1,4]

[1]Department of Physics, P.O. Box 43, FIN-00014, University of Helsinki, Finland

[2]Fachgebiet Materialmodellierung, Institut für Materialwissenschaft, TU Darmstadt, Otto-Berndt-Str. 3, D-64287 Darmstadt, Germany

[3]Helsinki Institute of Physics, P.O. Box 43, FIN-00014, University of Helsinki, Finland

[4]National Research Nuclear University MEPHI, Kashirskoe avenue, 31 Moscow, Russia

March 15, 2019

Abstract

In search of materials with better properties, polycrystalline materials are often found superior to their respective single crystalline counterparts. Reduction of grain size in polycrystalline materials can drastically alter the properties of materials, and when the grains reach nanometer scale, the improved mechanical response of the materials make them attractive in many applications. Multicomponent solid solution alloys have shown higher radiation tolerance compared to pure materials. Combining these both advantages, we investigate the radiation tolerance of nanocrystalline multicomponent alloys. We find that the alloys are able to withstand a much higher irradiation dose before the nanocrystallinity collapses, compared to nanocrystalline Ni. Some of the alloys managed to uphold their nanocrystallinity even twice as long as pure Ni.

*emil.levo@helsinki.fi

†fredric.granberg@helsinki.fi

1 Introduction

Single crystalline multi-principal element alloys have been found to exhibit many properties that have been sought after for various applications. So called high entropy alloys (HEAs) are a group of such alloys, consisting of at least five elements at roughly equal concentrations ($5 - 35\%$) [1, 2, 3]. For instance, HEAs have shown good corrosion and wear resistance [2], promising mechanical properties [2], thermal stability and hardness at high temperatures [2, 4, 5], good tensile strength at low temperatures [6], as well as improved ductility, fatigue, strength and fracture resistance [6, 7, 8]. These are all properties required in future nuclear applications, such as generation-IV reactors, which make HEAs candidate materials for the needs of nuclear power plants. In this respect, radiation tolerance is one of the main requirements to newly developed materials. Studies of radiation resistance of HEAs have yielded favourable results [9, 10, 11, 12, 13, 14]. For example a reduced defect growth, which has been observed in what can be seen as a subgroup of HEAs, so called equiatomic multicomponent alloys, or EAMC-alloys [10, 13].

Experimental studies thus far have been carried out on both single crystalline alloys as well as on polycrystalline materials [9, 11, 12, 15, 16]. In addition to the experimental investigations, computational studies have also been carried out on single crystals [10, 13, 14, 17, 18, 19]. However, while these results are directly comparable, from a practical viewpoint, single crystals are often very expensive and show high anisotropy of different properties, which is undesirable for most applications. Therefore, more research on polycrystalline HEA materials needs to be done. The simulations performed for single crystal materials can also be used for comparison with polycrystalline samples, if experimental observations are made within the grains, far from the grain boundaries. As the simulations are limited in size, the direct simulation of micrometer grains is impossible with conventional simulation techniques, used for irradiation simulations. However, the effect of the presence of a grain boundary can be investigated in nanocrystalline materials, where the average size of crystallites is of the order of a few nanometers.

The irradiation experiments on HEAs have in many cases focused on Ni-based alloys [10, 11, 15, 16, 18]. In addition, computer simulations have been carried out on the same alloys, in a variety of different interatomic potentials [10, 13, 18, 19] and it was seen that some of the alloys showed a superior performance compared to elemental Ni, under the same conditions.

In addition to conventional polycrystalline materials, with the grain sizes in the micrometer scale, nanocrystalline metallic systems have become an attractive option for structural materials, mainly due to their high strengths compared to polycrystalline and single crystalline alternatives [20, 21, 22, 23, 24, 25, 26]. For instance, nanocrystalline

Ni has shown a far higher strength, as the grain size is reduced from micrometers down to tens of nanometers [26]. The larger volume fraction of grain boundaries in nanocrystalline alloys obstruct dislocation motion, strengthening them, but at the same time posing as a vulnerability at higher temperatures [23]. This is why nanocrystalline HEAs, that are thermally more stable than conventional alloys, could be a good candidate for certain applications with harsh conditions, and have already been studied to some extent [23, 24, 25].

To study whether nanocrystalline HEAs are a feasible option for application in an irradiation environment, we have in this work studied the radiation stability of single phase nanocrystalline multicomponent alloys. We study alloys from the binary to quaternary composition, and compare them to a single element nanocrystalline sample. The nanocrystalline samples were subject to a similar irradiation scheme as in previous single crystal studies [10, 13], shown to yield comparable results with experiments [27]. We focus on several Ni-based alloys, as they have been showing good resistance to irradiation in single crystal form. In addition, nanocrystalline Ni samples have previously shown many desirable properties, as discussed in Ref. 26. We observe that nanocrystallinity persists in all the studied structures until a certain irradiation dose, when it collapses and the structure becomes single crystal. Such an abrupt transition was observed for the alloys in several interatomic potentials. We also studied the evolution of the grain structure, effect of composition as well as some of the intermediate defect structures during the irradiation.

2 Methods

2.1 Creating nanocrystalline simulation cells

The nanocrystalline samples were created using Voronoi tessellation [28, 29, 30] with around ten randomly chosen points inside the simulation cell. Each point corresponds to the center of a created grain. The Voronoi polyhedrons constructed are filled with a Face-centered cubic (FCC) lattice in random crystallographic orientation. Atoms of different types are distributed randomly on the created lattice sites to obtain the different alloy compositions given in Table I.

Each simulation cell of about 446 000 atoms contains 10 grains with an average grain radius of 5 nm resulting in a cubic simulation cell with the side length 17 nm. The cells in the present simulations are of the same size as used in [10, 13] where a similar irradiation scheme was applied. To ensure the statistical viability of our results, we created three simulation cells with the same size and number of grains, using different initial grain positions. This leads to different initial grain shapes and orientations. The three different cells are visualized in Fig. 1. These structures were

used as base for all nanocrystalline alloys, where the atoms were randomly replaced to achieve the correct overall ratio of different components. The random cells of all compositions were relaxed in the corresponding interatomic potentials with a Berendsen pressure control [31] to equilibrium and with a Berendsen temperature control to 300 K [31], which was the investigated temperature.

2.2 Irradiation simulations

The classical MD code PARCAS [32, 33] was utilized for all the irradiation simulations. Three different interatomic potentials were used to simulate multiple alloys, all of which are listed in Table I. We used the following interatomic potentials: Zhou *et al.* [34], Bonny *et al.* [35] and Purja Pun *et al.* [36]. The materials were chosen to correspond to earlier experiments and simulations on single crystalline samples [9, 10, 12, 19]. The Zhou *et al.* interatomic potential has been used to study the defect accumulation in single crystal materials containing up to 4 elements [10, 13, 14]. Moreover, it has been used to investigate the interplay of segregation and irradiation in the NiCoFeCu model HEA [17]. The Bonny *et al.* potential has also been used to study the irradiation of binary and ternary alloys [18, 19]. We used several interatomic potentials for the same materials as in Refs. 10, 13 and 14, to enable the comparison with previously obtained results, as well as to assess the differences in interatomic interaction models of different potentials. However, in the present studies we included the Ni_2Fe and Ni_3Fe to study any effect of Fe on the compositional stability of the nanocrystalline sample, and some alloys were excluded, since they were not stable in a nanocrystalline FCC lattice structure in the corresponding interatomic potential, see Sec. 3.

The irradiation scheme applied in the current study is similar as in Refs. 10 and 13. This scheme has been seen to yield comparable results with experiments for single crystalline samples, where experimental Rutherford Backscattering Spectroscopy in a channeling direction (RBS-C) spectra were compared with the ones obtained from the simulated results [27, 37]. In the following, we outline the main differences and main principals of the irradiation procedure. In the current simulations, we split the simulation of a single cascade in two steps. At first, we simulated a 5 keV recoil irradiation event with Berendsen thermostat [31], which was applied on atoms inside a 0.4 nm thin layer at all the sides of the simulation cell. Each recoil event was simulated for 20 ps, enough for the heat spike to cool down sufficiently. During this simulation step, an adaptive timestep was utilized to capture the correct trajectories [38] and an electronic stopping was applied as a friction force on all atoms with a kinetic energy over 1 eV. During the second step, a relaxation simulation was carried out with both Berendsen thermo- and barostats [31] on all atoms in the simulation cell. This relaxation simulation lasted for 10 ps and was sufficient

to cool the system down to 300 K and to reach a fairly uniform overall zero pressure in the simulation cell. As a result, no overheating or pressure buildup occurred during the whole simulation series. The recoil event was initiated in the middle of the simulation cell, in order to avoid an overlap with the thermally controlled borders. Then to achieve homogeneous irradiation, the cell was shifted randomly in three dimensions before initiating the next cascade simulation. This was repeated as many times as needed so that massively overlapping cascades were achieved, in our case until the nanocrystalline structure of the simulation cell fails, *i.e.* it collapses into some simpler phase.

2.3 Aging simulations

The binary nanocrystalline NiFe samples were annealed at elevated temperatures to study the phase stability under equilibrium conditions without irradiation. These simulations were carried out using the open source MD code LAMMPS [39, 40]. All cases of NiFe described by the Zhou *et al.* were subjected to this isothermal heat treatment at 800 K in the isobaric-isothermal (NPT) ensemble under pressure free conditions. To ensure chemical equilibration, we performed Monte Carlo steps in the semi-grand-canonical ensemble on 25 % of the atoms every 20 MD steps [41]. Similar parameters were used in Ref. 17. This Monte Carlo method requires the chemical potential difference $\Delta\mu_{i-j}$ of the different species as input parameter. The following $\Delta\mu_{i-j}$ value was used: NiFe: $\Delta\mu_{\text{Ni-Fe}} = -0.212\,\text{eV}$. This gave us the desired bulk concentrations. In total, each sample was annealed for 1 ns using a 1 fs timestep.

2.4 Analysis

The irradiated cells were mainly analyzed with the Open Visualization Tool OVITO [42]. The atomic structure of the simulation cells was studied throughout the simulations with the adaptive Common Neighbor Analysis (aCNA) modifier [43]. The CNA-modifier analyzes the amount of atoms in the following crystal structures: Face-centered cubic (FCC), hexagonal close-packed (HCP), body-centered cubic (BCC), icosahedral coordination (ICO) and other (unknown coordination structure). We observed that the grain boundaries in the nanocrystalline cells consisted mostly of atoms with an unidentified crystal structure (other), while the grain interiors of the unirradiated structures consisted of FCC atoms, that amounted to about 82 % of the total number of the atoms in the cell. During the massively overlapping cascades, the atoms in the simulation cell reorganize so heavily, that grains ultimately reorient, grain boundaries diminish and the structure of the whole simulation cell transforms into a more simple FCC phase or FCC/HCP-complex. Once the percentage of the atoms in the FCC environment grew over 90 in a simulation

cell, the simulation was stopped, as the cell had arguably lost its nanocrystallinity. We also analyzed the percentage of FCC and HCP atoms, since the atoms may reorganize in to an HCP structure, as the nanocrystallinity collapses. This might be required, since the energy difference between the FCC and HCP phases, in the materials described by the interatomic potentials used here, is rather small. We also investigated the volume change in the simulation cells, comparing them to perfect FCC cells, to make sure that if we see any drastic changes they should coincide with the phase transition into a simpler crystal structure during the prolonged irradiation.

In addition to the analysis of the threshold dose for the collapse of nanocrystallinity, we studied the formation of defects by determining the dislocation structures. The dislocation structures in the intermediate and resulting cells were analyzed with the Dislocation Extraction Algorithm (DXA) [44], also implemented in OVITO.

3 Results and Discussion

The typical grain evolution for the irradiated nanocrystalline cells can be seen in Fig 2, for Ni in all three interatomic potentials. During the massively overlapping cascades, the grain boundaries reorganize themselves into the most desirable crystal structure, which in most cases appears to be FCC. Piece by piece the grains that internally consist of FCC atoms merge, resulting in a decline in nanocrystallinity and emergence of an almost perfect FCC cell, except for remnant defects at the sites of initial grain boundaries and defects continuously introduced by the irradiation process. As is apparent in the figure, the grain evolution is fairly similar in the different potentials with the largest difference in the number of cascades, needed to reach a certain stage of damage evolution in the cells. Some structural differences observed for each cell can be explained by the use of different interatomic potentials, but to a larger extent they are due to the randomness of irradiation process and are not significant for the current analysis. Most importantly, we observe that the collapse of nanocrystallinity happens after very different number of cascades in the different potentials, this is why the results must be considered rather qualitatively than quantitatively. In addition, a quantitative comparison with the response of the single crystal cell, of the same elemental composition, cannot be done directly either. However, we can compare the dislocation structures in the nanocrytalline and single crystal cells qualitatively, which will be discussed later.

Fig. 3 shows the number of cascades for each composition, when the amount of FCC atoms has risen above 90 % ("criterion 1" and indicated by red, green and blue filled symbols) and when the amount of FCC+HCP atoms has risen above 90 % ("criterion 2" marked by grey filled symbols). The simulations that reach these collapse points,

are terminated shortly thereafter, since the structure had arguably have lost its nanocrystallinity. Some of the cases did not collapse at all, or only collapsed according to the second criterion, and are marked with open symbols. We stopped these simulations prematurely, as they had already shown the trend needed for this study. The three different initial structures used for the compositions are represented by different symbols, and referred to as the cases 1, 2 and 3 in the legend (see Fig. 1). In Fig. 4, we show the evolutions of the percentage of FCC atoms ((a)–(c)) and simulation cell volume ((d)–(f)) for "Case 1" (see Fig 1 (a)) against the number of cascades it has gone through. The plots in the upper (percentage of the FCC atoms) and lower (atomic volume) rows of Fig. 4 appear to be the mirror images of each other in terms of the increase, or decrease, of the relative amount of FCC atoms and volume, indicating that the phase reorganization has occurred.

Some of the investigated alloys that are not shown in Fig. 3 (that were mentioned earlier) did not follow the same trend in structural evolution. The materials in question were NiFe, NiCoFe and NiCoCr in the Zhou *et al.* potential. All these cells underwent phase transition from pure FCC to a mixture of FCC/BCC phases within the nanocrystallites during the prolonged irradiation. Since a single phase was not preserved, we excluded these structures from our analysis as we focused on single phase nanocrystalline alloys in the present work. Already after a few hundred cascades the FCC fraction had reduced drastically, while the BCC fraction rose. To investigate whether this was an effect of irradiation or the feature of the used potential, we performed aging simulations on the three unirradiated NiFe cells. These simulation confirmed the trend for the phase transition, which indicated that the phenomenon is due to the energetics of the composition rather than the irradiation. The aged cell of one of the initial structures can be seen in Fig. 5 (a), and the corresponding structure evolution can be seen in Fig. 5 (b). Analysis of the ground state energies at 0 K showed that the BCC phase was most favourable in the Zhou *et al.* potential for all three excluded alloys. However, in the Bonny *et al.* potential, the NiFe alloy is stable. This potential predicts the ground state for all concentrations of Fe in the NiFe alloy in the FCC phase [35], hence, the phase transition from FCC to BCC can hardly be expected in this potential. This is why we conclude that excluding the above-mentioned alloys from our analysis does not affect overall the conclusion of the present work.

From these figures it is obvious that elemental nanocrystalline Ni is the least stable material in all interatomic potentials. Any additional element stabilizes the structure making it more resistant to the irradiation. It is also apparent that the concentration and type of added element play important roles. For example, NiCo clearly improves the stability of the nanocrystalline cell in both the Zhou *et al.* and the Purja Pun *et al.* potential, but a further increase of the number of alloying elements (NiCoCu) decreases the stability in the Zhou *et al.* potential. The

fourth component, Fe, in the EAMC alloy (NiCoFeCu), marginally improves the stability of the nanocrystalline structure compared to NiCo. The impact of the concentration of secondary elements can be seen by comparing the different Ni_xFe samples, that were simulated in the Zhou *et al.* and the Bonny *et al.* potentials. In both potentials, the addition of a quarter or a third of Fe to Ni improves the stability of the nanocrystalline structure. However, from our results it is not clear which of the two alloys, Ni_3Fe or Ni_2Fe, is more stable, since in at least one case the results are opposite in the Zhou *et al.* and Bonny *et al.* potentials, implying that the physics described by these potentials is not sufficiently accurate to capture such a distinction.

The overall trend, in which order specific structures lose their nanocrystallinity, is consistent for most of the studied materials. The structure that collapses the earliest has usually the structure "Case 2", while "Case 3" lost its nanocrystallinity at the highest number of cascades. This implies that not only the size, but also the crystallographic orientation and shape of the grains greatly impacts the stability of the grain structure, which the most clearly seen in the Ni_2Fe sample in the Zhou *et al.* potential where there is a huge difference in the number of cascades needed to reach a 90 percentile FCC structure for the three different cases.

The defect structures found in the grains during the prolonged irradiation might be a reason for the different behavior in nanocrystalline stability. In the work by Levo *et al.* [13] the dislocation structures due to massively overlapping cascades were studied in similar EAMC alloys and elemental Ni, but using single crystal cells and only the Zhou *et al.* potential. Significantly greater amount of stacking fault tetrahedra (SFTs) were found in elemental Ni and in the binary alloy NiCo compared to more complex alloys. By this reasoning, one might expect to find more SFTs within the grains of nanocrystalline Ni and NiCo as well, compared to other alloys.

In Fig. 6 we show the snapshots of irradiation simulations of the "Case 2" elemental Ni structure in the Zhou *et al.* potential and NiFe in the Bonny *et al.* potential. The figure shows the interior structures of the irradiated nanocrystalline cells. Similar snapshots of "Case 2" of the rest of the materials in all potentials can be seen in the supplementary material available online. The images in the Zhou *et al.* potential were taken after 500 cascades, Bonny *et al.* potential after 1500 cascades and Purja Pun potential after 1000 cascades. These specific cascade numbers were chosen so that the cells have already been irradiated sufficiently long for SFTs to form, yet so that the nanocrystalline structure of these materials has not collapsed. Especially Ni in the Zhou *et al.* potential should at this point have a higher number of SFTs than more complex alloys according to Ref. 13. Note that in the figures, blue surfaces denote a defect mesh, red spheres HCP atoms, while empty space consists mostly of FCC atoms. We can clearly see a greater number of SFTs in one of the larger grains of the Ni cell, when compared with the other

materials, as was expected.

SFTs have been observed before in irradiated Ni and binary NiFe systems in the Bonny *et al.* potential [19]. We can see SFTs forming as well in the grains of our cells in Ni and all Ni_xFe alloys, but in a somewhat truncated form than those seen in the Zhou *et al.* potential. In the Bonny *et al.* potential there is not an as clear difference in the formed SFTs in the different materials as in the other potentials. The irradiated cells in the Purja Pun *et al.* potential also show SFTs in their grains, albeit more clearly in Ni than in NiCo.

In Fig. 7 one can see the defect structures found in structure "Case 1" for all materials in the Zhou *et al.* potential, after the loss of nanocrystallinity. Structure "Case 1" was chosen, since in many cases of the other structures the defects were obscured by stacking faults that had survived the transition from nanocrystallinity. We see fairly similar defect structures in all materials: Stacking faults surrounded by Shockley partial dislocations, SFTs outlined by stair-rod dislocations and defect clusters. When comparing the Ni and NiCo cells (Figs. 7 (a) and (d)) with equally irradiated, initially single crystalline cells [13], we see similar defect structures. The most notable difference is that no large Frank loops are present in our initially nanocrystalline cells, like they were in the irradiated cells in Ref. 13. This might imply that the grain boundaries dictate the kind of defect structures that are possible to form and survive during prolonged irradiation in nanocrystalline materials.

Fig. 8 shows the defect structures found in "Case 1" for all materials, in the Bonny *et al.* (Fig. 8 (a)-(d)) and Purja Pun *et al.* (Fig. 8 (e)-(f)) potentials, after the loss of nanocrystallinity. In the Bonny *et al.* potential we can see mostly similar defect structures to those found in the Zhou *et al.* potential, except for a couple of very large stacking faults in Ni_2Fe and NiFe that might be remnant structures of the grain boundaries that are case specific. A lot of SFTs can still be observed, complying with results in Ref. 19. In the Purja Pun *et al.* potential we see again fairly similar defect structures as before, only maybe less Shockley partial dislocations.

To compare these results with previous ones, further irradiation of the originally nanocrystalline structures is needed, even after a collapse, to see if they show the same long term response. In principle, these formerly nanocrystalline cells should yield the same evolution as the single crystal structures when irradiated, as they collapsed to almost perfect FCC. However, as described in the next paragraph, they became a bit larger in volume after the collapse, indicating that they are vacancy rich, which could affect the defect evolution. When studying these images, one needs to keep in mind that the different materials are not quantitatively comparable, since they have not been irradiated equally much.

An additional curiosity worth mentioning is the volume of the formerly nanocrystalline cells. Fig. 4 show that

the final volumes of the cells are for all materials in all potentials $1\% - 4\%$ larger than in respective pure FCC cells with the corresponding number of atoms. This might indicate an imbalance of interstitial atoms and vacancies in the systems, due to the initial nanocrystallinity and presence of large amount of grain boundaries. As the interstitials and vacancies have different mobilities, the interstitials can easily migrate to the grain boundaries, leaving the vacancies within the grains [45]. As seen in Fig. 6 and in the figures in the supplementary material online, there is only a very small number of dislocations in the centre of the grain, excluding the vacancy rich SFTs. This indicates that the produced dislocations easily can recombine with the grain boundaries. This results in a higher number of SFTs, that are immobile, and other vacancy type defect structures in the grains.

4 Conclusions

In this work we have found that all studied multicomponent nanocrystalline alloy structures are more stable under prolonged irradiation compared to elemental nanocrystalline Ni. The grain evolution during the irradiation seemed similar for the different potentials, with the biggest difference in how large an irradiation dose was needed to reach the collapse of the nanocrystallinity. The addition of elements showed an overall improvement from elemental Ni for three different potentials and initial structures. When comparing the EAMC-alloys with each other, it became obvious that a greater number of elements does not guarantee increased stability, since the nanocrystallinity persisted till a higher irradiation dose in binary NiCo than ternary NiCoCu. The different concentrations of added elements also showed an effect on the stability, but different results were obtained when comparing two of the potentials, thus indicating a need for further studies. The overall order in which the different structures lost their nanocrystallinity agrees mostly between the potentials. The three nanocrystalline structures collapsed at different points during irradiation, showing the significance of the initial geometries of the nanosized grains. The defect structures in irradiated cells of initially nanocrystalline Ni and NiCo structures in the Zhou *et al.* potential are found to be similar to those in equally irradiated single crystal cells. One exception is Frank dislocation loops, which were found in the single crystalline samples but not in the nanocrystalline samples, indicating a size dependence of the types of defects emerging from irradiation. Similarities in defect structures were also found for Ni and the NiFe binary alloys in the Bonny *et al.* potential when compared to previous work.

Acknowledgements

Grants of computer time from CSC – the Finnish IT Center for Science are gratefully acknowledged. This work has been partly carried out within the framework of the EUROfusion Consortium and has also received partial funding from the Euratom research and training programme 2014–2018 under grant agreement No 633053. The views and opinions expressed herein do not necessarily reflect those of the European Commission. D.U. and K.A. acknowledge financial support by the Deutsche Forschungsgemeinschaft (DFG) through project Grant No. STU 611/2-1 as part of SPP 2006. F.D. acknowledges partial support by Competitiveness Growth Program of the Federal Autonomous Educational Institution of Higher Professional Education National Research Nuclear University MEPhI.

References

[1] J.-W. Yeh, S.-K. Chen, S.-J. Lin, J.-Y. Gan, T.-S. Chin, T.-T. Shun, C.-H. Tsau, and S.-Y. Chang. Nanostructured high-entropy alloys with multiple principal elements: novel alloy design concepts and outcomes. *Adv. Eng. Mater.*, 6(5):299–303, 2004.

[2] M.-H. Tsai and J.-W. Yeh. High-entropy alloys: A critical review. *Mat. Res. Lett.*, 2(3):107–123, 2014.

[3] D. B. Miracle and O. N. Senkov. A critical review of high entropy alloys and related concepts. *Acta Mater.*, 122:448–511, 2017.

[4] M.-H. Chuang, M.-H. Tsai, W.-R. Wang, S.-J. Lin, and J.-W. Yeh. Microstructure and wear behavior of $Al_xCo_{1.5}CrFeNi_{1.5}Ti_y$ high-entropy alloys. *Acta Mater.*, 59(16):6308 – 6317, 2011.

[5] C.-Y. Hsu, C.-C. Juan, W.-R. Wang, T.-S. Sheu, J.-W. Yeh, and S.-K. Chen. On the superior hot hardness and softening resistance of $AlCoCr_xFeMo_{0.5}Ni$ high-entropy alloys. *Mater. Sci. Eng.: A*, 528(10):3581 – 3588, 2011.

[6] B. Gludovatz, A. Hohenwarter, D. Catoor, E. H. Chang, E. P. George, and R. O. Ritchie. A fracture-resistant high-entropy alloy for cryogenic applications. *Science*, 345(6201):1153–1158, 2014.

[7] Y. Wei, Y. Li, L. Zhu, Y. Liu, X. Lei, G. Wang, Y. Wu, Z. Mi, J. Liu, and H. Wang. Evading the strength – ductility trade-off dilemma in steel through gradient hierarchical nanotwins. *Nat. Commun.*, 5:3580, 2014.

[8] B. Gludovatz, A. Hohenwarter, K. V. S. Thurston, H. Bei, Z. Wu, E. P. George, and R. O. Ritchie. Exceptional damage-tolerance of a medium-entropy alloy CrCoNi at cryogenic temperatures. *Nat. Commun.*, 7:10602, 2016.

[9] Y. Zhang, G. M. Stocks, K. Jin, C. Lu, H. Bei, B. C. Sales, L. Wang, L. K. Béland, R. E. Stoller, G. D. Samolyuk, M. Caro, A. Caro, and W. J. Weber. Influence of chemical disorder on energy dissipation and defect evolution in concentrated solid solution alloys. *Nat. Commun.*, 6:8736, 2015.

[10] F. Granberg, K. Nordlund, M. W. Ullah, K. Jin, C. Lu, H. Bei, L. M. Wang, F. Djurabekova, W. J. Weber, and Y. Zhang. Mechanism of radiation damage reduction in equiatomic multicomponent single phase alloys. *Phys. Rev. Lett.*, 116(13):135504, 2016.

[11] S. Q. Xia, X. Yang, T. F. Yang, S. Liu, and Y. Zhang. Irradiation resistance in Al_xCoCrFeNi high entropy alloys. *J. Min. Met. & Mat. Soc.*, 67(10):2340–2344, 2015.

[12] Y. Zhang, K. Jin, H. Xue, C. Lu, R. J. Olsen, L. K. Beland, M. W. Ullah, S. Zhao, H. Bei, D. S. Aidhy, G. D. Samolyuk, L. Wang, M. Caro, A. Caro, G. M. Stocks, B. C. Larson, I. M. Robertson, A. A. Correa, and W. J. Weber. Influence of chemical disorder on energy dissipation and defect evolution in advanced alloys. *J. Mater. Res.*, 31(16):2363–2375, 2016.

[13] E. Levo, F. Granberg, C. Fridlund, K. Nordlund, and F. Djurabekova. Radiation damage buildup and dislocation evolution in Ni and equiatomic multicomponent Ni-based alloys. *J. Nucl. Mater.*, 490:323–332, 2017.

[14] F. Granberg, F. Djurabekova, E. Levo, and K. Nordlund. Damage buildup and edge dislocation mobility in equiatomic multicomponent alloys. *Nucl. Inst. Meth. Phys. Res. Sec. B*, 393:114 – 117, 2017.

[15] N. A. P. Kiran Kumar, C. Li, K. J. Leonard, H. Bei, and S. J. Zinkle. Microstructural stability and mechanical behavior of FeNiMnCr high entropy alloy under ion irradiation. *Acta Mater.*, 113:230 – 244, 2016.

[16] C. Lu, L. Niu, N. Chen, K. Jin, T. Yang, P. Xiu, Y. Zhang, F. Gao, H. Bei, S. Shi, M.-R. He, I. M. Robertson, W. J. Weber, and L. Wang. Enhancing radiation tolerance by controlling defect mobility and migration pathways in multicomponent single-phase alloys. *Nat. Commun.*, 7:13564, 2016.

[17] L. Koch, F. Granberg, T. Brink, D. Utt, K. Albe, F. Djurabekova, and K. Nordlund. Local segregation versus irradiation effects in high-entropy alloys: Steady-state conditions in a driven system. *J. Appl. Phys.*, 122(10):105106, 2017.

[18] G. Velisa, M. W. Ullah, H. Xue, K. Jin, M. L. Crespillo, H. Bei, W. J. Weber, and Y. Zhang. Irradiation-induced damage evolution in concentrated Ni-based alloys. *Acta Mater.*, 135:54 – 60, 2017.

[19] M. W. Ullah, H. Xue, G. Velisa, K. Jin, H. Bei, Wi. J. Weber, and Y. Zhang. Effects of chemical alternation on damage accumulation in concentrated solid-solution alloys. *Sci. Rep.*, 7(1):4146, 2017.

[20] H. Van Swygenhoven and J. R. Weertman. Deformation in nanocrystalline metals. *Mater. Today*, 9(5):24 – 31, 2006.

[21] M. A. Meyers, A. Mishra, and D. J. Benson. Mechanical properties of nanocrystalline materials. *Prog. Mater. Sci.*, 51(4):427 – 556, 2006.

[22] K. Lu, L. Lu, and S. Suresh. Strengthening materials by engineering coherent internal boundaries at the nanoscale. *Science*, 324(5925):349–352, 2009.

[23] Y. Zou, J. M. Wheeler, H. Ma, P. Okle, and R. Spolenak. Nanocrystalline high-entropy alloys: a new paradigm in high-temperature strength and stability. *Nano Lett.*, 17(3):1569–1574, 2017.

[24] W. Liao, S. Lan, L. Gao, H. Zhang, S. Xu, J. Song, X. Wang, and Y. Lu. Nanocrystalline high-entropy alloy $CoCrFeNiAl_{0.3}$ thin-film coating by magnetron sputtering. *Thin Solid Films*, 638:383–388, 2017.

[25] K. M. Youssef, A. J. Zaddach, C. Niu, D. L. Irving, and C. C. Koch. A novel low-density, high-hardness, high-entropy alloy with close-packed single-phase nanocrystalline structures. *Mat. Res. Lett.*, 3(2):95–99, 2015.

[26] F. Ebrahimi, G. R. Bourne, M. S. Kelly, and T. E. Matthews. Mechanical properties of nanocrystalline nickel produced by electrodeposition. *Nanostruct. Mater.*, 11(3):343 – 350, 1999.

[27] S. Zhang, K. Nordlund, F. Djurabekova, F. Granberg, Y. Zhang, and T. S. Wang. Radiation damage buildup by athermal defect reactions in nickel and concentrated nickel alloys. *Mater. Res. Lett.*, 5(6):433–439, 2017.

[28] G. Voronoi. Nouvelles applications des paramètres continus à la théorie des formes quadratiques. premier mémoire. sur quelques propriétés des formes quadratiques positives parfaites. *J. Reine Angew. Math. (Crelle's Journal)*, 1908(133), 1908.

[29] G. Voronoi. Nouvelles applications des paramètres continus à la théorie des formes quadratiques. deuxième mémoire. recherches sur les paralléloèdres primitifs. *J. Reine Angew. Math. (Crelle's Journal)*, 1908(134), 1908.

[30] G. Voronoi. Nouvelles applications des paramètres continus à théorie des formes quadratiques. deuxième mémoire. recherches sur les paralléloèdres primitifs. *J. Reine Angew. Math. (Crelle's Journal)*, 1909(136), 1909.

[31] H. J. C. Berendsen, J. P. M. Postma, W. F. van Gunsteren, A. DiNola, and J. R. Haak. Molecular dynamics with coupling to external bath. *J. Chem. Phys.*, 81(8):3684, 1984.

[32] K. Nordlund, M. Ghaly, R. S. Averback, M. Caturla, T. Diaz de la Rubia, and J. Tarus. Defect production in collision cascades in elemental semiconductors and FCC metals. *Phys. Rev. B*, 57(13):7556–7570, 1998.

[33] K. Nordlund, J. Keinonen, M. Ghaly, and R. S. Averback. Coherent displacement of atoms during ion irradiation. *Nature*, 398(6722):49–51, 1999.

[34] X. W. Zhou, R. A. Johnson, and H. N. G. Wadley. Misfit-energy-increasing dislocations in vapor-deposited CoFe/NiFe multilayers. *Phys. Rev. B*, 69:144113, 2004.

[35] G. Bonny, N. Castin, and D. Terentyev. Interatomic potential for studying ageing under irradiation in stainless steels: the FeNiCr model alloy. *Mod. Sim. Mat. Sci. Eng.*, 21(8):085004, 2013.

[36] G. P. Purja Pun, V. Yamakov, and Y. Mishin. Interatomic potential for the ternary Ni-Al-Co system and application to atomistic modeling of the B2-$L1_0$ martensitic transformation. *Mod. Sim. Mat. Sci. Eng.*, 23(6):065006, 2015.

[37] S. Zhang, K. Nordlund, F. Djurabekova, Y. Zhang, G. Velisa, and T. S. Wang. Simulation of Rutherford backscattering spectrometry from arbitrary atom structures. *Phys. Rev. E*, 94:043319, 2016.

[38] K. Nordlund. Molecular dynamics simulation of ion ranges in the 1 – 100 keV energy range. *Comput. Mater. Sci.*, 3:448, 1995.

[39] S. Plimpton. Fast parallel algorithms for short-range molecular dynamics. *J. Comput. Phys.*, 117(1):1–19, 1995.

[40] LAMMPS Molecular Dynamics Simulator `lammps.sandia.gov`.

[41] B. Sadigh, P. Erhart, A. Stukowski, A. Caro, E. Martinez, and L. Zepeda-Ruiz. Scalable parallel Monte Carlo algorithm for atomistic simulations of precipitation in alloys. *Phys. Rev. B*, 85(18), 2012.

[42] A. Stukowski. Visualization and analysis of atomistic simulation data with OVITO - the Open Visualization Tool. *Mod. Sim. Mat. Sci. Eng.*, 18(1):015012, 2010.

[43] A. Stukowski. Structure identification methods for atomistic simulations of crystalline materials. *Mod. Sim. Mat. Sci. Eng.*, 20(4):045021, 2012.

[44] A. Stukowski, V. V. Bulatov, and A. Arsenlis. Automated identification and indexing of dislocations in crystal interfaces. *Mod. Sim. Mat. Sci. Eng.*, 20(8):085007, 2012.

[45] S. Zhao, G. M. Stocks, and Y. Zhang. Defect energetics of concentrated solid-solution alloys from ab initio calculations: $Ni_{0.5}Co_{0.5}$, $Ni_{0.5}Fe_{0.5}$, $Ni_{0.8}Fe_{0.2}$ and $Ni_{0.8}Cr_{0.2}$. *Phys. Chem. Chem. Phys.*, 18(34):24043–24056, 2016.

List of Figures

1 The three initial structures. Atoms with FCC structure are colored blue, and atoms in any other structure are colored white. The atoms are identified using adaptive Common Neighbor Analysis (cf. Sec. 2.4). 20

2 Grain evolution and final defect structures in pure Ni for all three potentials (Zhou *et al.* on top, Bonny *et al.* in the middle and Purja Pun *et al.* on the bottom). Snapshots taken from key points in FCC evolution (see Fig. 4 upper row). The number found in the captions are the number of cascades initiated in the simulation cell. 21

3 The number of cascades that resulted in the collapse of nanocrystallinity for each corresponding composition of the alloys. Open symbols show the results of the prematurely stopped simulations, which showed the trend needed for this study. The differently shaped symbols (square, circle and triangle) indicate different initial structures ("Case 1", "Case 2" and "Case 3"), see Fig. 1. The red, blue and green filled symbols represent points at which the fraction of FCC atoms in the system has grown over 90%, while the grey filled symbols represent points at which the fraction of FCC+HCP atoms in the system has grown over 90%. 22

4 Graphs showing the FCC percentage ((a)–(c)) and volume ((d)–(f)) evolution in structure "Case 1" for each material in all three applied potentials. The volume is divided by the volume of a perfect FCC cell with an equal amount of atoms. 23

5 The aging of NiFe "Case 2". The colors represent different crystal structures as follows: Green – FCC, blue – BCC, red – HCP, yellow ICO and white – OTHER (black in (b) for visibility). 24

6 Defect structures in the irradiated nanocrystalline cells. The upper row after 500 cascades for Ni in the Zhou *et al.* potential and the lower row after 1500 cascades for NiFe in the Bonny *et al.* potential. 25

7 Defect structures in structure "Case 1" for all materials in the Zhou *et al.* potential. 26

8 Defect structures in structure "Case 1" for all materials in the Bonny *et al.* ((a)-(d)) and the Purja Pun *et al.* ((e)-(f)) potential. 27

List of Tables

I The simulated materials (left-most column) with corresponding potentials (top row). If no numbers are indicated, the alloys have an equal fraction of all elements. 29

List of Figures

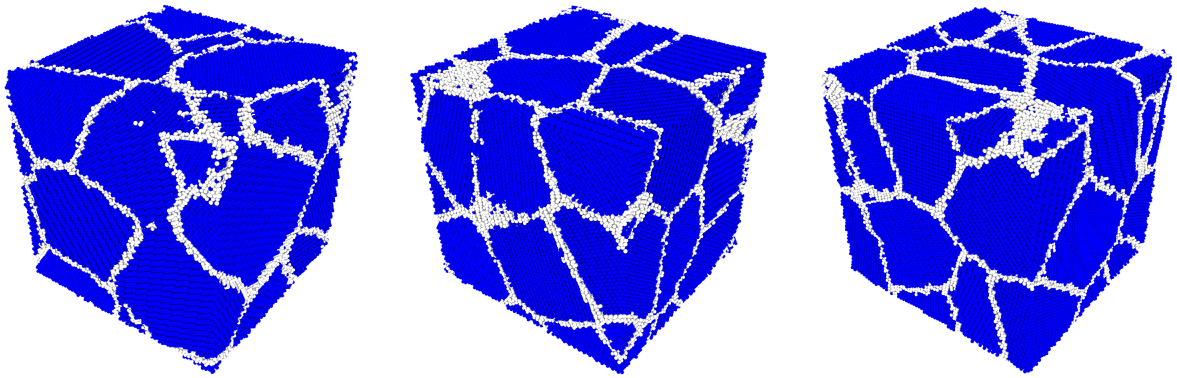

(a) Case 1 (b) Case 2 (c) Case 3

Figure 1: The three initial structures. Atoms with FCC structure are colored blue, and atoms in any other structure are colored white. The atoms are identified using adaptive Common Neighbor Analysis (cf. Sec. 2.4).

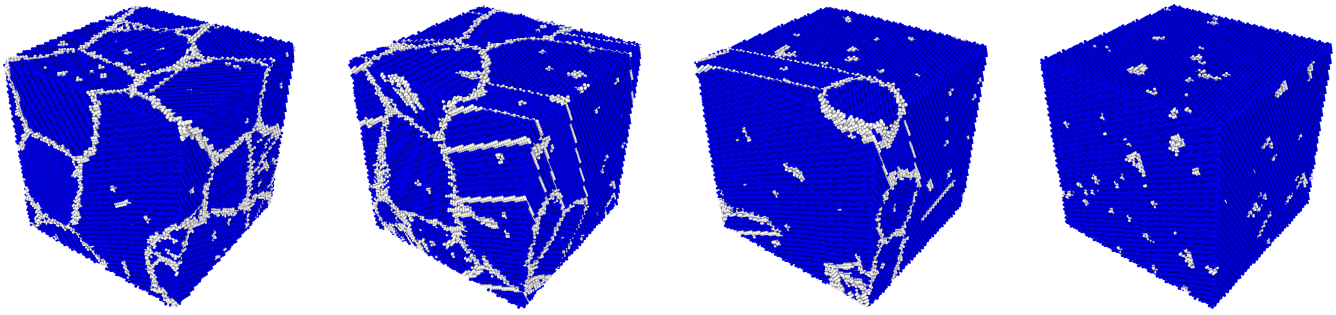

(a) Zhou *et al.* after 200 cascades

(b) Zhou *et al.* after 1100 cascades

(c) Zhou *et al.* after 1200 cascades

(d) Zhou *et al.* after 1300 cascades

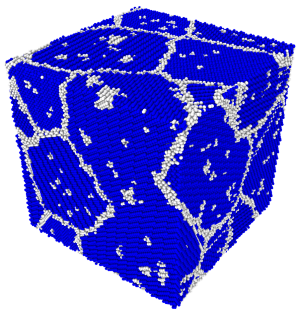

(e) Bonny *et al.* after 1000 cascades

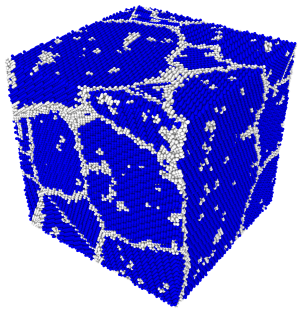

(f) Bonny *et al.* after 2500 cascades

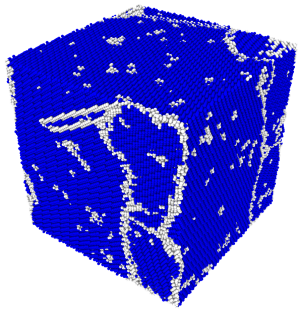

(g) Bonny *et al.* after 2900 cascades

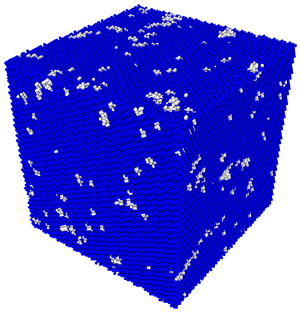

(h) Bonny *et al.* after 3100 cascades

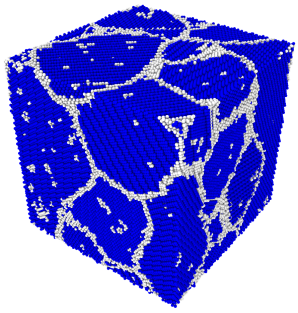

(i) Purja Pun *et al.* after 400 cascades

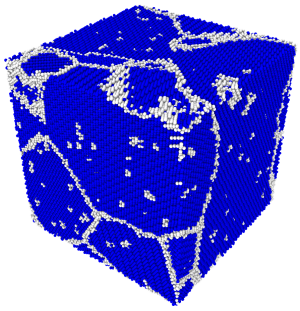

(j) Purja Pun *et al.* after 1900 cascades

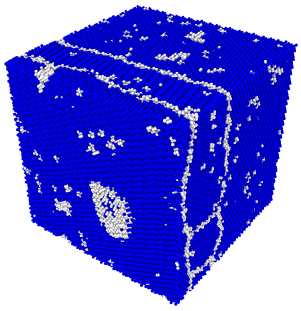

(k) Purja Pun *et al.* after 2300 cascades

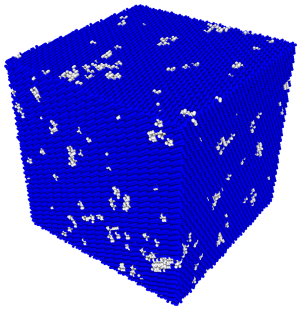

(l) Purja Pun *et al.* after 2600 cascades

Figure 2: Grain evolution and final defect structures in pure Ni for all three potentials (Zhou *et al.* on top, Bonny *et al.* in the middle and Purja Pun *et al.* on the bottom). Snapshots taken from key points in FCC evolution (see Fig. 4 upper row). The number found in the captions are the number of cascades initiated in the simulation cell.

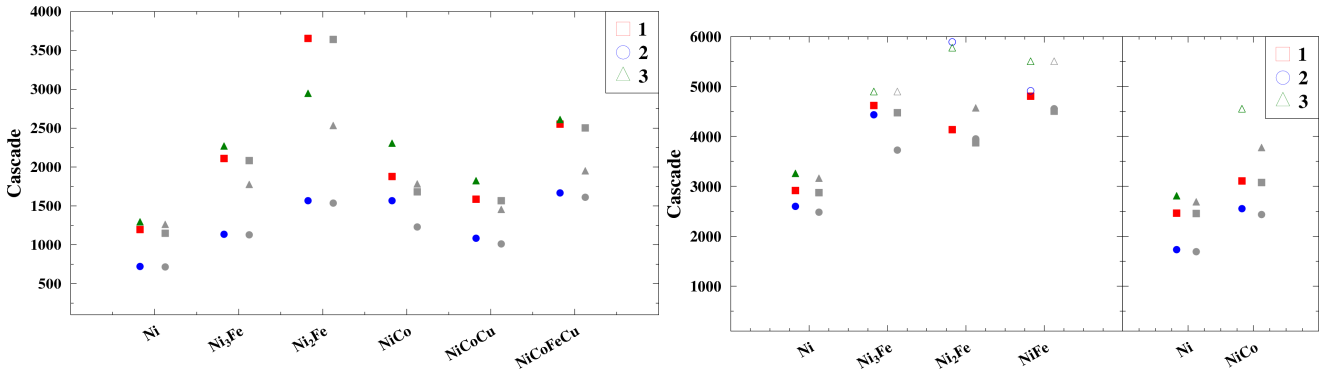

(a) Zhou *et al.*

(b) Bonny *et al.* (left) and Purja Pun *et al.* (right)

Figure 3: The number of cascades that resulted in the collapse of nanocrystallinity for each corresponding composition of the alloys. Open symbols show the results of the prematurely stopped simulations, which showed the trend needed for this study. The differently shaped symbols (square, circle and triangle) indicate different initial structures ("Case 1", "Case 2" and "Case 3"), see Fig. 1. The red, blue and green filled symbols represent points at which the fraction of FCC atoms in the system has grown over 90%, while the grey filled symbols represent points at which the fraction of FCC+HCP atoms in the system has grown over 90%.

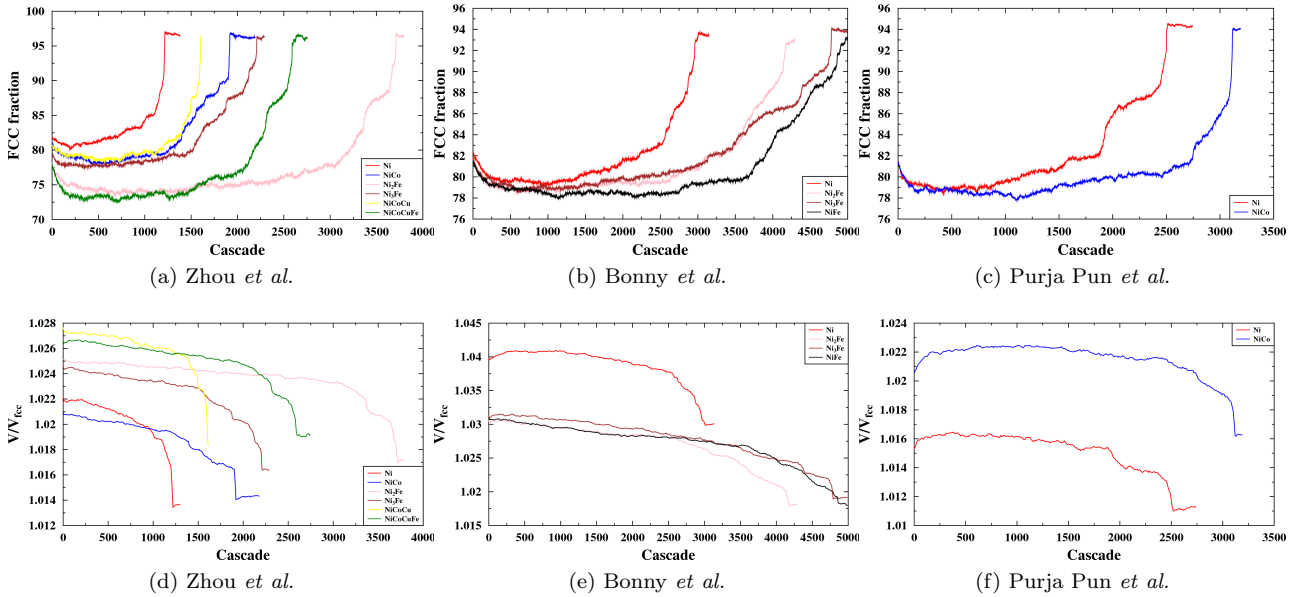

(a) Zhou *et al.* (b) Bonny *et al.* (c) Purja Pun *et al.*

(d) Zhou *et al.* (e) Bonny *et al.* (f) Purja Pun *et al.*

Figure 4: Graphs showing the FCC percentage ((a)–(c)) and volume ((d)–(f)) evolution in structure "Case 1" for each material in all three applied potentials. The volume is divided by the volume of a perfect FCC cell with an equal amount of atoms.

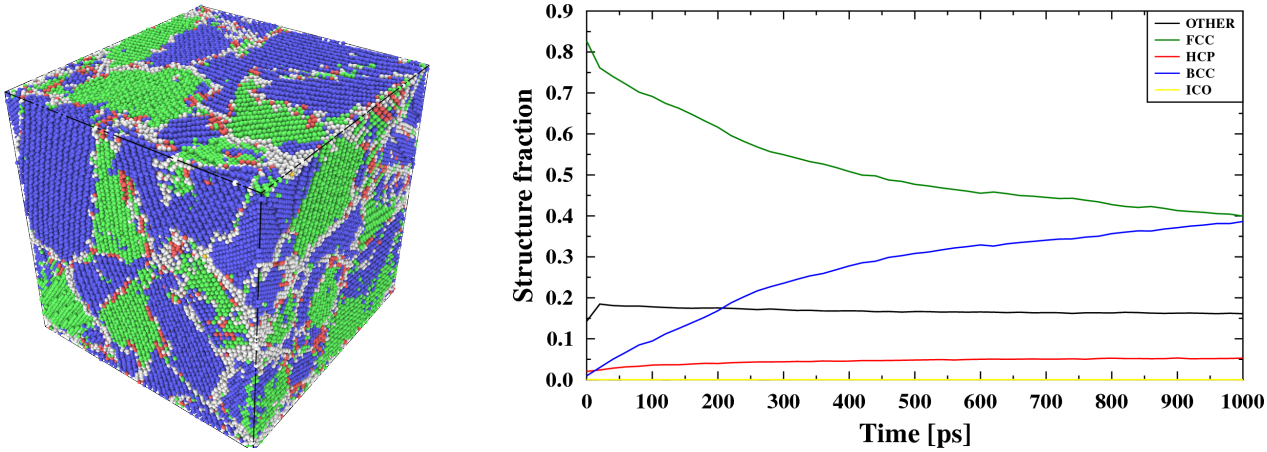

(a) Aged NiFe "Case 2" cell.

(b) The evolution of the different phases during aging.

Figure 5: The aging of NiFe "Case 2". The colors represent different crystal structures as follows: Green – FCC, blue – BCC, red – HCP, yellow ICO and white – OTHER (black in (b) for visibility).

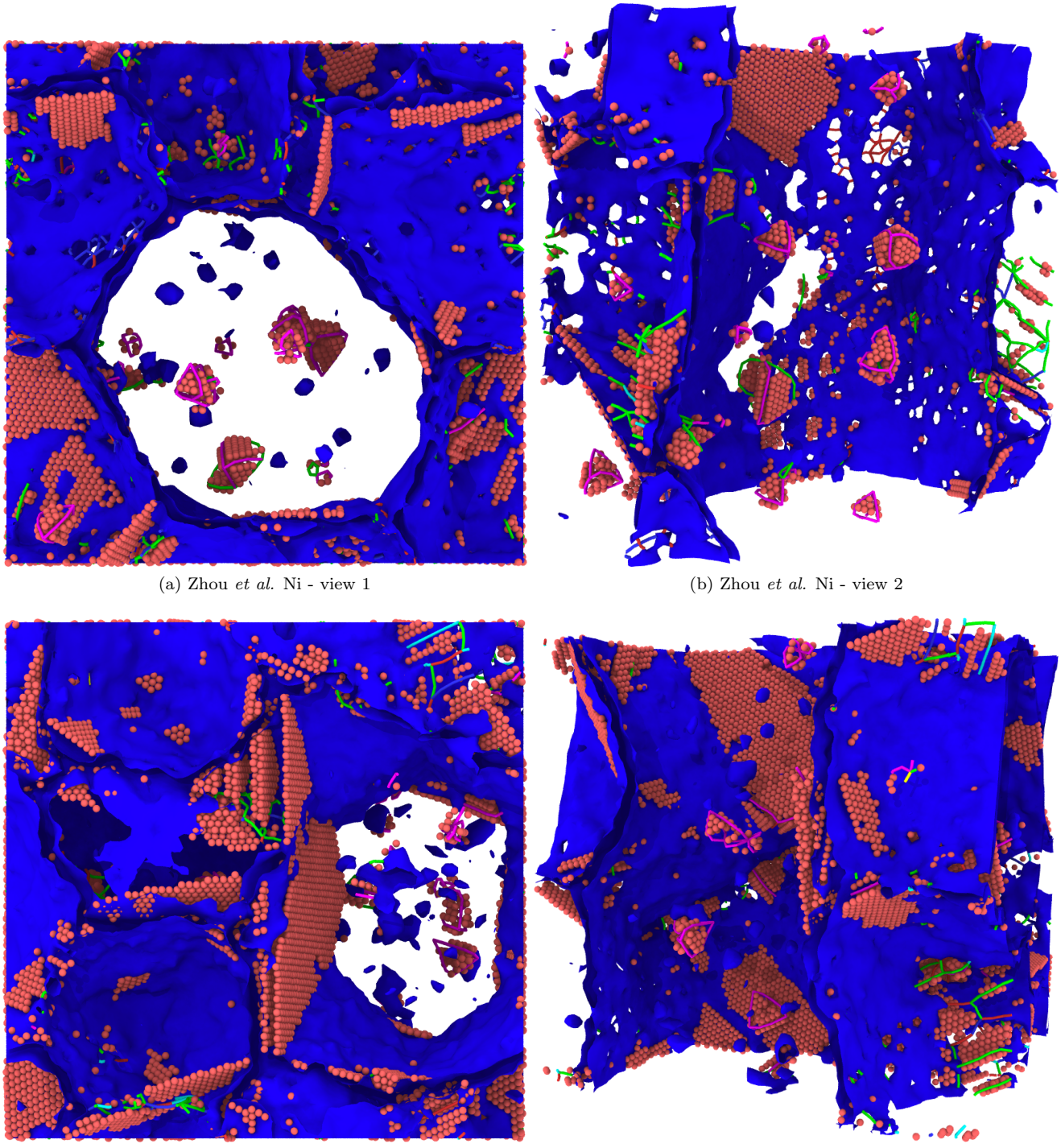

(a) Zhou *et al.* Ni - view 1

(b) Zhou *et al.* Ni - view 2

(c) Bonny *et al.* NiFe - view 1

(d) Bonny *et al.* NiFe - view 2

Figure 6: Defect structures in the irradiated nanocrystalline cells. The upper row after 500 cascades for Ni in the Zhou *et al.* potential and the lower row after 1500 cascades for NiFe in the Bonny *et al.* potential.

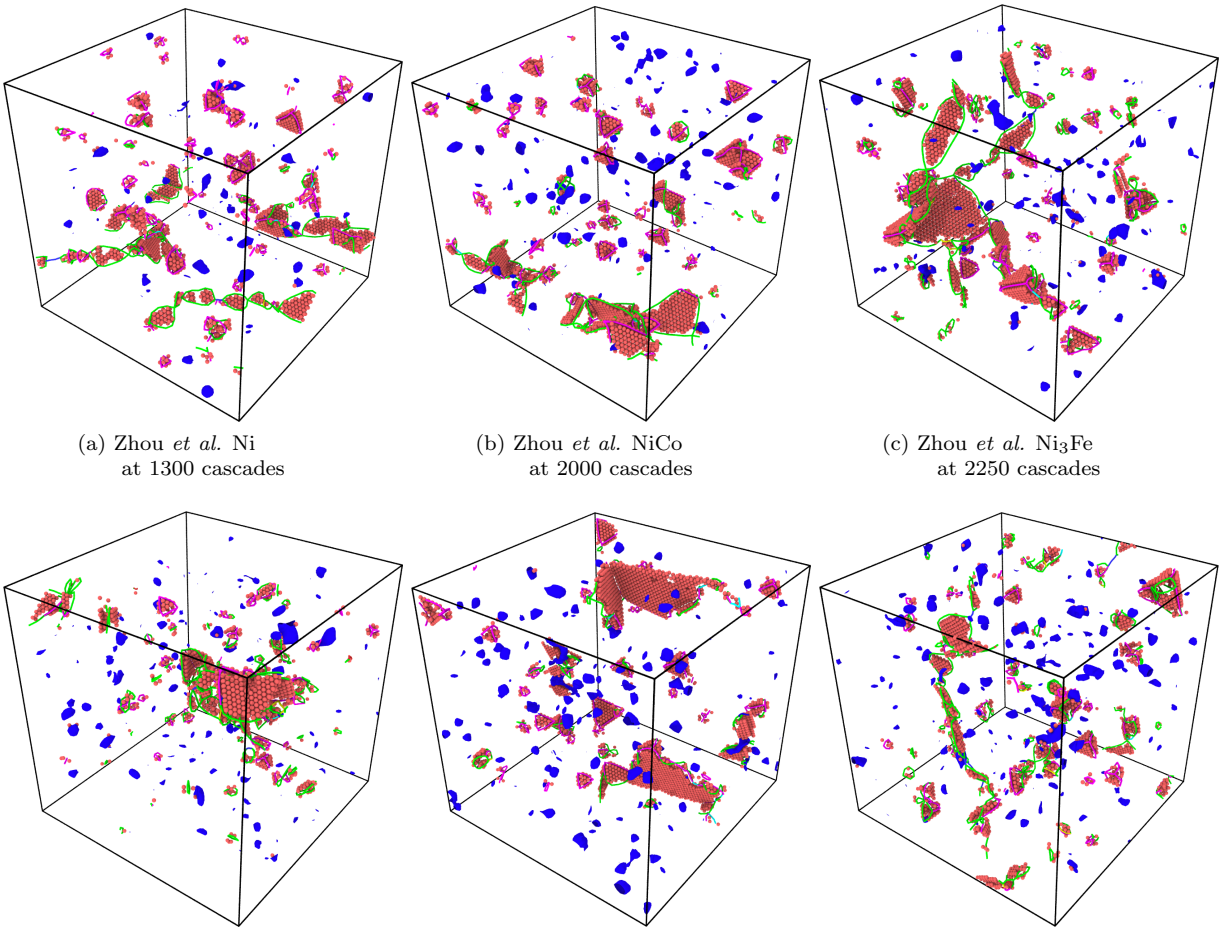

(a) Zhou *et al.* Ni at 1300 cascades

(b) Zhou *et al.* NiCo at 2000 cascades

(c) Zhou *et al.* Ni_3Fe at 2250 cascades

(d) Zhou *et al.* Ni_2Fe at 3750 cascades

(e) Zhou *et al.* NiCoCu at 1610 cascades

(f) Zhou *et al.* NiCoFeCu at 2750 cascades

Figure 7: Defect structures in structure "Case 1" for all materials in the Zhou *et al.* potential.

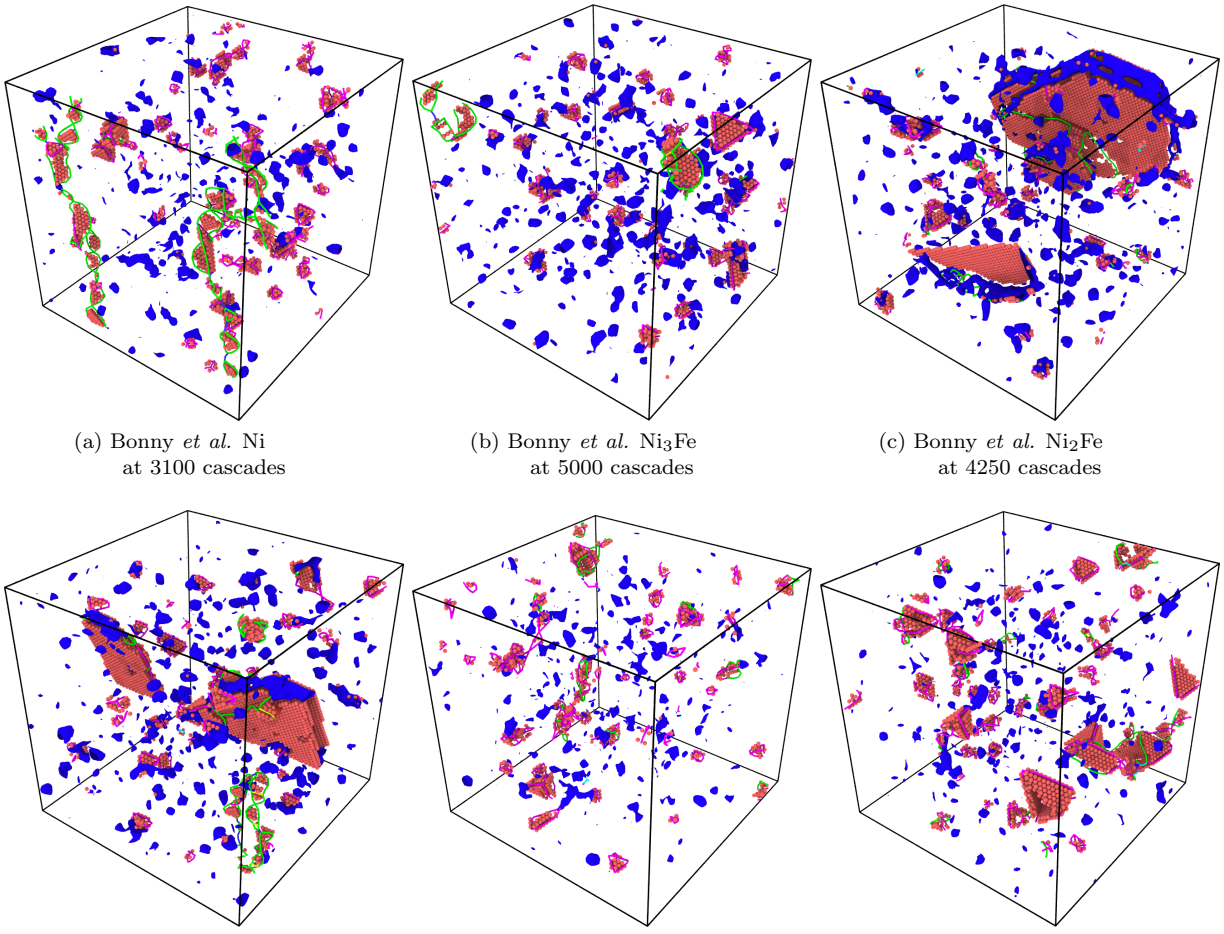

(a) Bonny *et al.* Ni at 3100 cascades

(b) Bonny *et al.* Ni_3Fe at 5000 cascades

(c) Bonny *et al.* Ni_2Fe at 4250 cascades

(d) Bonny *et al.* NiFe at 5000 cascades

(e) Purja Pun *et al.* Ni at 2740 cascades

(f) Purja Pun *et al.* NiCo at 3195 cascades

Figure 8: Defect structures in structure "Case 1" for all materials in the Bonny *et al.* ((a)-(d)) and the Purja Pun *et al.* ((e)-(f)) potential.

List of Tables

	Zhou *et al.*	Bonny *et al.*	Purja Pun *et al.*
Ni	✓	✓	✓
NiCo	✓		✓
Ni_2Fe	✓	✓	
Ni_3Fe	✓	✓	
NiFe		✓	
NiCoCu	✓		
NiCoFeCu	✓		

Table I: The simulated materials (left-most column) with corresponding potentials (top row). If no numbers are indicated, the alloys have an equal fraction of all elements.